SCIENCE CHINA
Chemistry

•FEATURE ARTICLES•

https://doi.org/10.1007/s11426-024-2266-8

Applications of *in-situ* solid-state nuclear magnetic resonance (ssNMR) in methanol to olefins (MTO) reaction

Jing Niu[1,2], Shutao Xu[1,2,3*], Yingxu Wei[1,2,3] & Zhongmin Liu[1,2,3]

[1]*National Engineering Research Center of Lower-Carbon Catalysis Technology, Dalian Institute of Chemical Physics, Chinese Academy of Sciences, Dalian 116023, China;*
[2]*State Key Laboratory of Catalysis, Dalian Institute of Chemical Physics, Chinese Academy of Sciences, Dalian 116023, China;*
[3]*University of Chinese Academy of Sciences, Beijing 100049, China*

Received July 16, 2024; accepted August 20, 2024; published online August 30, 2024

The methanol-to-olefins (MTO) reaction offers an alternative pathway for the production of low-carbon olefins from non-oil feedstocks. Fundamental research has been impeded by a lack of comprehensive understanding of its underlying mechanism, despite the significant progress made in industry. *In-situ* solid-state nuclear magnetic resonance (ssNMR) spectroscopy has emerged as a pivotal tool, offering crucial insights into key species under real-time *operando* conditions. Furthermore, the host–guest interaction between zeolites or surface species residing on zeolites and the reactant/active intermediates is revealed by the combination of *in-situ* ^{13}C MAS NMR and 2D correlation spectroscopy. Moreover, recent technological advancements in hyperpolarization (HP) methods, including HP ^{129}Xe NMR and dynamic nuclear polarization (DNP), have significantly improved the sensitivity of ssNMR, enabling detailed structural and kinetic analysis as well as the detection of trace species. In this feature article, we summarized recent advancements in (*in-situ*) ssNMR spectroscopy applied to MTO reaction processes, encompassing mechanistic investigations at various stages and the intricate host–guest interactions. These theoretical insights into the dynamic evolution of MTO reactions lay a solid foundation for the optimization of catalytic processes and the development of efficient catalysts, thereby advancing the techniques towards more sustainable and economical production route for olefins.

MTO, zeolites, *in-situ* ssNMR, reactive intermediates, reaction mechanism

Citation: Niu J, Xu S, Wei Y, Liu Z. Applications of *in-situ* solid-state nuclear magnetic resonance (ssNMR) in methanol to olefins (MTO) reaction. *Sci China Chem*, 2024, 67, https://doi.org/10.1007/s11426-024-2266-8

1 Introduction

Since its discovery by Mobil in 1977 [1], methanol-to-olefins (MTO) has been the primary catalytic process for producing light olefins from non-oil feedstocks, such as coal, natural gas, biomass, and CO_2. This process has received tremendous attention from both academia and industry due to its unprecedented industrial application value [2]. In 2010, the first commercialization of MTO for producing olefins from coal-based methanol, namely DMTO technology, was successfully realized by Dalian Institute of Chemical Physics (DICP), Chinese Academy of Sciences. This has opened up a new field for the sustainable production of olefins from abundant non-petrochemical resources. As of 2024, the development of the second generation (DMTO-II) and third generation (DMTO-III) process with a combined olefin capacity of 21.6 Mt/year has been successfully accomplished.

Understanding the mechanism of MTO is crucial for improving catalyst efficiency, reducing process costs, and de-

Published in virtual special issue "Advanced Characterization Techniques in Catalysis"
*Corresponding author (email: xushutao@dicp.ac.cn)

veloping efficient catalysts with better performance. Due to their unique acidic and well-defined channel/cavity structure, zeolites have been one of the most widely used catalysts in industry, especially in the MTO process [3–5]. During the reaction process, the acidity and structure of zeolites interact with the products, intermediates, and transition states at various stages of the MTO reaction, resulting in dynamic and complex characteristics of the mechanism of MTO. The MTO reaction generally consists of three stages: the initial stage, the highly-efficient steady-state stage, and the deactivation stage [6–8]. Describing how the first C–C bond formation occurs in the initial stage has been a long-standing issue[9,10]. Additionally, the formation of alkenes from the generation of C–C bond accelerates the MTO reaction, leading to intricate reaction networks in the steady-state stage. In the deactivation stage, the elucidation of the evolution and distribution of coke species inside zeolites is vitally important, as it directly affects the catalyst lifespan and product selectivity [11]. Importantly, at all stages of MTO reaction, the covalent and non-covalent interactions between inorganic zeolite and organic reactants/intermediates/products play an assignable role in influencing the adsorption and diffusion of reactants/products, manipulating the formation and transformation of intermediates/transition states, regulating the reaction pathways, and reversibly adjusting the structure of zeolites [12]. Therefore, the *in-situ* monitoring of the dynamic reaction mechanism at different stages is crucial for a comprehensive understanding of the reaction.

In-situ ssNMR spectroscopy is a powerful method for obtaining fundamental information about the dynamic evolution of entire species during real reaction conditions with high time resolution [13–16]. This technique provides multiscale information from static to dynamic, including the adsorption and evolution of reactants/intermediates, the formation and diffusion of products, and the host–guest interactions between the reactants/intermediates with the zeolite framework during the MTO process. In this feature article, we briefly summarize our recent work on understanding the dynamic mechanism and the host–guest interaction in the MTO process by *in-situ* magic angle spinning (MAS) NMR techniques. This article comprises the following parts: (1) an overview of the available *in-situ* ssNMR methods for studying the MTO reaction; (2) the application of ssNMR spectroscopy, especially *in-situ* methods, on the dynamic mechanism in each stage of the MTO process; (3) the host–guest interaction revealed by the advanced ssNMR spectroscopy in the MTO reaction. Finally, based on these significant contributions to the deepening of the understanding of the entire process at the molecular level, an outlook is provided along with expected future developments in the field of *in-situ* ssNMR technique for zeolites.

2 Introduction of *in-situ* ssNMR methods utilized in MTO process

Over the years, significant progress has been made in ssNMR, including developing pulse sequences [15,17], high magnetic field technology [18], and hyperpolarization (HP) methods [19,20] to enhance the sensitivity and resolution of ssNMR spectroscopy. To provide accurate mechanistic information under reaction conditions, ssNMR methods have been designed to accommodate diverse real reaction environments, including batch-like conditions, continuous-flow conditions, high-pressure conditions, and even extreme experimental conditions such as combining high-pressure and high/low temperature. In this article, we will therefore concentrate mostly on the *in-situ* MAS NMR techniques employed in mechanistic studies of MTO reactions.

2.1 *In-situ* MAS NMR under batch-like conditions

There are two general experimental approaches for conducting *in-situ* MAS NMR experiments under batch-like conditions. The first approach uses a sealed, highly symmetrical glass insert that fits within a MAS rotor, essentially serving as a microreactor [21–24]. Following the loading of pre-activated catalyst particles and adsorbents into the glass ampoules, these glass ampoules are flame-sealed under vacuum. Then, after a designated heating period, the reaction is promptly quenched using liquid nitrogen before transferring the sealed glass ampoules into the MAS rotor for measurement at room temperature. The glass ampoule fits into a standard commercial 7 mm MAS rotor, which limits the spinning rate to not surpass 5 kHz, impacting the spectral resolution to some degree. Despite being considered a quasi-*in-situ* technique, this method offers several distinct advantages. First, it can be implemented on commercial instruments without modifications to probes and rotors. Second, the ruggedness of the glass insert allows it to withstand elevated pressures, with reported pressures of up to 20 MPa. Finally, this approach proves to be more cost-effective than continuous-flow techniques (the introduction can be found in the following text), and furnishes insights on multiple stages of the reaction, including adsorption of reactants, formation of intermediates, and conversion to products.

Another approach is based on the application of gas tight MAS NMR rotors which need to be prepared using a special vacuum line apparatus. Several types of apparatus have been designed to seal and unseal MAS rotors directly on a vacuum line. For example, Haw and co-workers [24] designed the cryogenic adsorption vessel enabling rotor nestling (CAVERN) to facilitate catalyst evacuation, loading of reactants, and sealing of the rotor in a single device. With this apparatus, solid catalysts can be activated up to 1,100 K under

vacuum and exposed to reactants *in situ*. The catalyst and adsorbents can then be transferred to a commercial MAS rotor and sealed using rotor caps with deformable ridges that create air-tight seals upon insertion. This method avoids handling activated catalysts in a glove box, simplifying the sample preparation. Additionally, the CAVERN apparatus enables easy manipulation of reactions at low temperatures by transferring the rotor filled with catalysts and reactants into a pre-cooled variable-temperature (VT) MAS NMR probe. These apparatuses are versatile for abroad temperature range of approximately 300–1,000 K, and suitable for both batch and continuous-flow conditions.

2.2 *In-situ* MAS NMR under continuous-flow conditions

The industrial process of MTO is usually carried out under flow conditions. Different protocols, including continuous-flow (CF), switched-flow, stopped-flow, and pulsed-flow experiments have been developed for *in-situ* flow MAS NMR experiments by manipulating the temperature and flow gas during the reaction [24–27]. Haw and co-workers [28] designed a pulse quench catalytic reactor to reveal the mechanism of methanol conversion on H-ZSM-5 under conditions identical to conventional flow reactors. The catalyst was fixed in a microreactor as a catalyst bed, and ^{13}C-methanol with continuous helium carrier gas was injected onto the bed at 643 K. Following a rapid quenching from the reaction temperature, the volatile products were analyzed by gas chromatography (GC), and the organic species on the catalyst were cooled by cryogenically cooled nitrogen and then characterized by ssNMR at room temperature. This protocol allows for the observation of stable cyclopentenyl cations under flow conditions. In 1995, Hunger and co-workers [29] used an NMR rotor as a microreactor to conduct *in-situ* MAS NMR under CF conditions. The carrier gas loaded with reactant vapors was injected into the interior of the cylindrical catalyst bed in the spinning MAS NMR rotor. The reactants flow from the bottom to the top inside the MAS NMR rotor, and the product stream exits the rotor through an annular gap in the rotor cap. In some cases, the reaction products can be transferred to a peripheral analytical system (such as a GC or mass spectrometer) by connecting a pump. In 2009, as depicted in Figure 1, we have developed a new approach that combines *in-situ* laser-hyperpolarized (HP) ^{129}Xe MAS NMR with ^{13}C MAS NMR to study the catalytic kinetics of MTO under flow conditions [25]. The HP ^{129}Xe is generated by the optical pumping and then mixed with a reactant outside the probe head before entering the MAS NMR rotor located with the catalyst. This method significantly increased the signal intensity of HP ^{129}Xe by 4–5 orders of magnitude, allowing us to monitor the catalytic process at an early stage with much higher sensitivity and in a shorter acquisition time. Consequently, the reaction intermediates can be identified by ^{13}C MAS NMR. Meanwhile, the kinetic and dynamic process of methanol adsorption and conversion in nanocages can be monitored by one- and two-dimensional HP ^{129}Xe MAS NMR under CF conditions. Therefore, the CF *in-situ* MAS NMR technique has significant advantages, such as monitoring the initial adsorption processes of reactants onto catalysts and capturing the highly reactive species that are only present during the reaction conditions.

3 Applications of ssNMR spectroscopy on MTO process

Typically, the MTO process involves the initial stage, the steady-state stage, and the deactivation stage, with a very dynamic and complex reaction mechanism. Advanced ssNMR spectroscopy, especially *in-situ* techniques, provides straightforward information at the atomic/molecular scale for the entire MTO process, including the local structure and

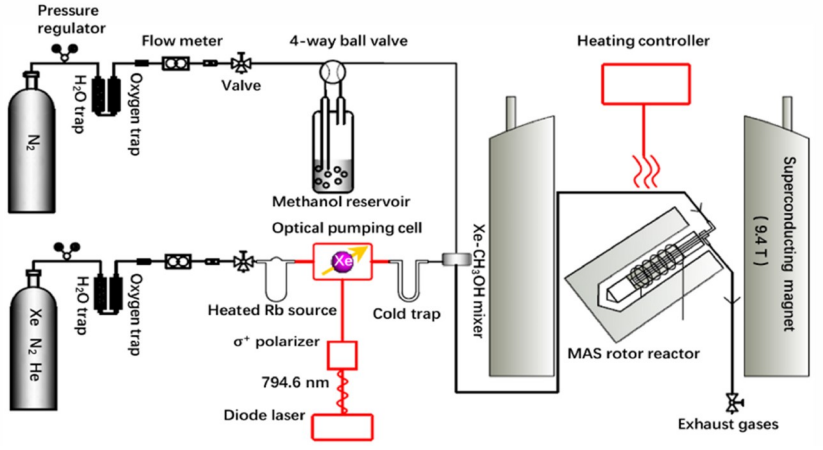

Figure 1 (Color online) Schematic representation of the experimental setup for *in-situ* MAS NMR coupled with HP ^{129}Xe under continuous-flow conditions [25]. Adapted with permission from ref. 25, Copyright 2009 American Chemical Society.

active sites of zeolites, the mechanistic information of the dynamic reaction process, the adsorption and diffusion of reactants/products, and the host–guest interaction of zeolite-based catalytic systems.

3.1 Revealing the dynamic direct mechanism for the formation of the first C–C bond in the initial stage of MTO reaction

In the initial reaction stage, the formation of the first C–C bond is one of the key scientific issues. The controversy over the direct mechanism and indirect mechanism has been ongoing for many years [8–10,30]. Since the 1970s, more than 20 direct mechanisms have been proposed to explain the coupling of C–C bond from C1 species, including the methyl cation, surface methoxy species (SMS), carbene, oxonium ylides, and even a methane–formaldehyde complex [7,31–34]. However, the lack of convincing experimental evidence for the real intermediates or transition state, along with the lack of theoretical evidence, led to the common assumption that traces of impurities in the feedstocks, carrier gas, or catalysts were the source of the first C−C bond for a long time [35]. Owing to the extremely high reactivity and low coverage of the potential intermediates on the catalyst surface, obtaining experimental evidence for the occurrence and transformation of the real intermediates/species at the very initial stage under MTO reaction conditions remains challenging. With the development of multiple spectroscopic techniques, the possibility of a direct mechanism as the initial C–C bond generation has been reported by several groups since 2016. For example, our group utilized the *in-situ* ^{13}C MAS NMR and variable temperature one-dimensional (1D) and two-dimensional (2D) correlation spectra to elucidate the dynamic process of the first C–C bond formation from SMS [36–39]. Deng's group [40] verified the high reactivity of the SMS bounded to an extra-frame-work Al (EFAL) and proposed an EFAL-assisted route for the formation of the first C–C bond. Meanwhile, the direct mechanism centered on SMS has also been verified by the research groups of Hunger [9,41], Fan [42], Guan [43], Kondo [34], Lercher [44], and Weckhuysen [45]. In this section, we focused on our recent work that constructs a complete pathway for the C–C bond formation with the help of *in-situ* ^{13}C MAS NMR technique under real/quasi-reaction conditions.

3.1.1 In-situ spectroscopic evidence of a direct mechanism for the formation of the first C–C bond

In 2017, we employed *in-situ* ssNMR spectroscopy under continuous-flow conditions to investigate the initial stage of methanol conversion over HZSM-5 zeolite at the reaction temperature of 573 K [46]. As shown in Figure 2, we observed the presence of SMS ($\delta_{^{13}C}$ = 59.5 ppm) and trimethyloxonium TMO ($\delta_{^{13}C}$ = 80.0 ppm), along with a surface methyleneoxy analogue ($\delta_{^{13}C}$ = 69.0 ppm) derived from activated dimethyl ether (DME) was first observed under the reaction conditions. Notably, this signal was only detected under the *operando* reaction conditions. The ^{13}C chemical shift prediction by GIPAW periodic method further confirmed the ^{13}C NMR chemical shift towards the low field when stretching the distance of C–H bonds of the DME, indicating the polarization of the C–O bond for methyleneoxy analogue. Additionally, the significant peak broadening of the methyleneoxy analogue suggests a strong interaction between the activated DME species and either the catalyst or active surface groups (e.g., SMS, TMO) formed on Brønsted acid sites (BAS). Our findings offer compelling experimental evidence for a synergetic mechanism of direct C–C bond formation from SMS/TMO-mediated DME/methanol activation during the initial stage of the MTO reaction.

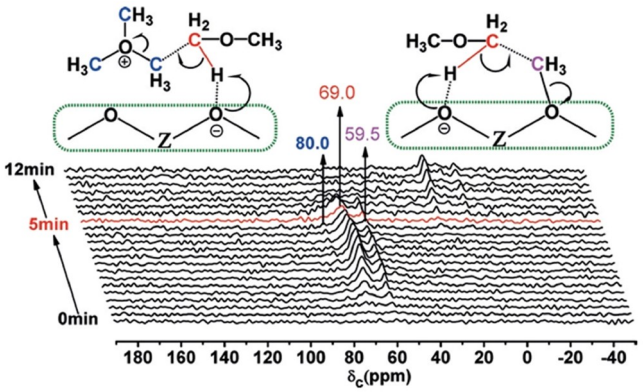

Figure 2 (Color online) *In-situ* solid-state ^{13}C MAS NMR spectra recorded during ^{13}C-methanol conversion over HZSM-5 at 573 K. The spectra were recorded every 20 s from 0 to 5 min and then every 60 s from 5 to 12 min [46]. Adapted with permission from ref. 46, Copyright 2017 Wiley-VCH GmbH.

3.1.2 Identification of the interaction between SMS and DME/methanol

Based on the above findings, we further provided precise evidence for the interaction between the adsorbed reactant and the intermediate using 2D ^{13}C–^{13}C correlation spectroscopy [36]. To observe the spatial proximity and interaction in the very initial stage, the MTO reaction was stopped after the reaction at 573 K for 60 s. The catalyst was then quickly quenched by liquid nitrogen and transferred into the NMR rotor for ^{13}C NMR measurement. This *ex-situ* method is suitable for capturing the surface species in a fast reaction system that can hardly be investigated by *in-situ* NMR methods due to the limited temporal resolution of solid sample analysis by NMR. Consisting with the previous research, we found that SMS was the only newly formed surface species detected at the very beginning of the MTO reaction, suggesting that SMS is the critical intermediate for the first C–C bond formation. The conventional 2D proton-

driven spin diffusion (PDSD) is a homonuclear correlation technique for reintroducing the internal spin interactions under MAS conditions. The cross-peaks in the PDSD experiment provide information on internuclear distances. Figure 3 shows the ^{13}C–^{13}C PDSD ssNMR spectra of the catalyst recorded with a mixing time of 150 ms at various temperatures of 298, 353, and 403 K. No cross-peak was observed at 298 K. As the temperature increased to 353 K, the cross-peak between SMS (56.7 ppm) and DME (60.5) appeared. This correlation was enhanced significantly at 403 K, and a new correlation between SMS and methanol (50.8) was captured, suggesting close spatial proximity and a stronger interaction at this temperature. These results provide strong experimental evidence for the formation of the initial C–C bond from the direct coupling of SMS and the surface-adsorbed C1 reactant (Scheme 1).

The 2D ^{13}C–^{13}C combined $R2_v^n$-driven (CORD) spin diffusion experiments are also very powerful for determining the intermolecular interactions of surface species during MTO reactions on zeolites. After the MTO reaction for 20 s at 573 K on HZSM-5-90 (Si/Al = 90), the 2D ^{13}C–^{13}C CORD MAS NMR correlation spectroscopy (Figure 4) provided direct evidence of the SMS-mediated methanol pathway for generating the initial C–C bond [38]. The spatial proximity between DME and SMS was observed by the appearance of a correlation peak at (58.5, 59.6) ppm, reflecting a strong intermolecular interaction between C1 species. It is worth noting that no cross-peaks between methanol and the SMS were detected, which differs from the capture of the correlations between the surface adsorbed methanol/DME with the SMS on SAPO-34. Combined with the *operando* advanced ab initio molecular dynamics (AIMD) simulation and projected density of state (PDOS) analysis, we demonstrated that the C–H bond of DME was more deeply activated than that of methanol by the SMS, resulting in an SMS-mediated DME pathway (with the free energy barrier of 154 kJ mol^{-1}) energetically favored over the SMS-mediated methanol pathway (with the free energy barrier of 184 kJ mol^{-1}) for generating the initial C–C bond.

Based on experimental and theoretical evidence, SMS was proposed to act as a methylating agent in MTO reactions. However, the complicacy and instantaneity of the MTO reaction obscure the catalytic behaviors of C1 reactant molecules under the real MTO reaction condition [31]. In 2021, with the help of *in-situ* ssNMR spectroscopy, we directly

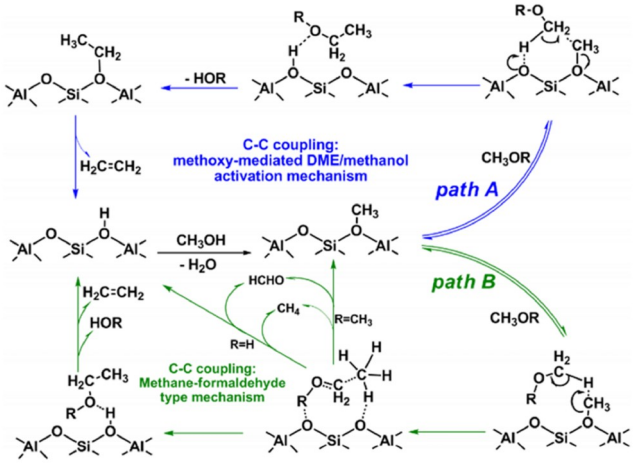

Scheme 1 (Color online) Plausible reaction pathways for the formation of the earliest-detected hydrocarbons during the initial stage of the MTO reaction [36]. Adapted with permission from ref. 36, Copyright 2018 American Chemical Society.

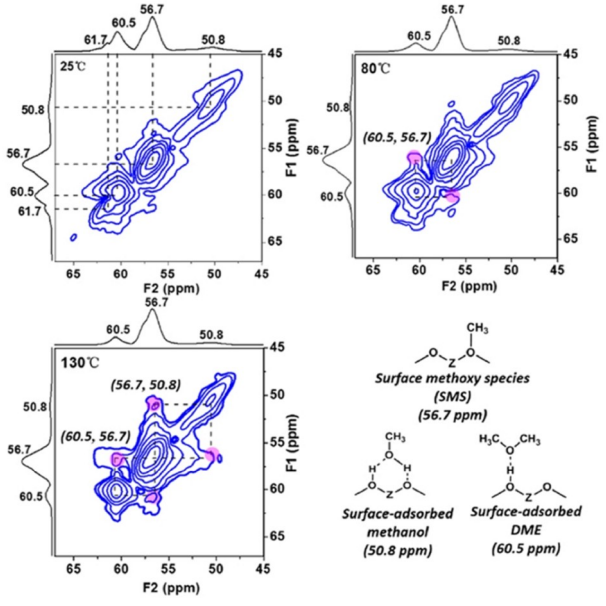

Figure 3 (Color online) ssNMR correlations of SMS, DME, and methanol on HSAPO-34. 2D ^{13}C–^{13}C MAS NMR spectra with a mixing time of 150 ms are recorded at 298, 353, and 403 K after the MTO reaction for 60 s at 573 K [36]. Adapted with permission from ref. 36, Copyright 2018 American Chemical Society.

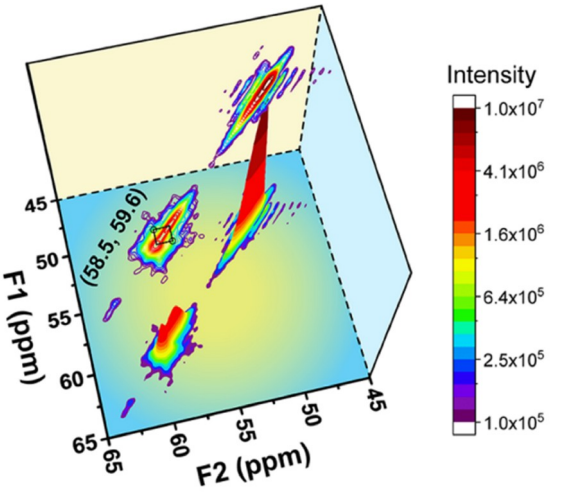

Figure 4 (Color online) 2D ^{13}C–^{13}C CORD spin diffusion MAS NMR correlation spectra (recorded at 298 K) for C1 species on HZSM-5-90 after MTO reaction for 20 s at 573 K [38]. Adapted with permission from ref. 38, Copyright 2021 American Chemical Society.

revealed the progressive activation of dimethyl ether (DME) evoked by the special catalysis from CH_3-Zeo [39]. Figure 5a shows the *in-situ* ^{13}C MAS NMR spectra recorded upon the conversion of $^{13}CH_3OH$ in an NMR rotor reactor under continuous-flow conversion over HZSM-5 at programmed temperatures increasing from 373 to 573 K. After the formation of the hybrid supramolecular catalytic system initiated by SMS, the chemical shift of DME gradually shifted from 63.5 to 69.0 ppm as the temperature was increased from 473 to 573 K, indicating that the highly activated DME exhibits the nature of the methyleneoxy analogue species (CH_3–O–$CH_2^{\delta-}$–$H^{\delta+}$). Additionally, the rate of formation of initial olefins is consistent with the increasing trend of chemical shifts of DME (Figure 5b), which means that the progressive activation of approaching DME leads to the formation of initial hydrocarbons. With *operando* AIMD simulations, we speculate that the C−O bond varies from covalent bonding to ionic bonding as the temperature increases from 273 to 773 K, leading to the dynamic activation of DME due to the gradually enhanced electrophilicity of $CH_3^{\delta+}$. Based on these spectroscopy and simulation results, we provided the first case of dynamic activation of C1 molecules by the CH_3-Zeo catalytic system in the very initial period of the MTO process (Figure 5c).

3.1.3 *Elucidation of the whole first C–C bond formation process of the MTO reaction over chabazite zeolite*

Recently, we employed *in-situ* ssNMR measurements and 2D ^{13}C–^{13}C correlation spectroscopy experiments to clarify the dynamic reaction process and real-time interactions of C1 species in the very early stage of the MTO process [37]. By conducting CF ^{13}C-methanol conversion over HSSZ-13 in a rotor reactor at 493 K, surface ethoxy species (SES) was identified as the highly reactive ethene precursor from real-time monitored ^{13}C MAS NMR spectroscopy (Figures 6a and 6b). During the conversion of ^{13}C-methanol, the signals of surface-adsorbed/bound methanol (50.2 ppm), SMS (58.5 ppm), and DME (60.5 ppm) are easily distinguished. A new signal at 68.5 ppm with low intensity was only observable in this *in-situ* experiment at the very initial MTO reaction stage. Considering the previous result on HZSM-5, this signal was attributed to an important surface methyleneoxy analog species. To slow down the activation step, we further conducted the MTO reaction at a relatively low reaction temperature and characterized the cooled catalyst after ^{13}C-methanol conversion at room temperature. For the first time, we directly captured the highly reactive SES in the real MTO reaction, whose structure was unambiguously established according to the correlation peak pair between the

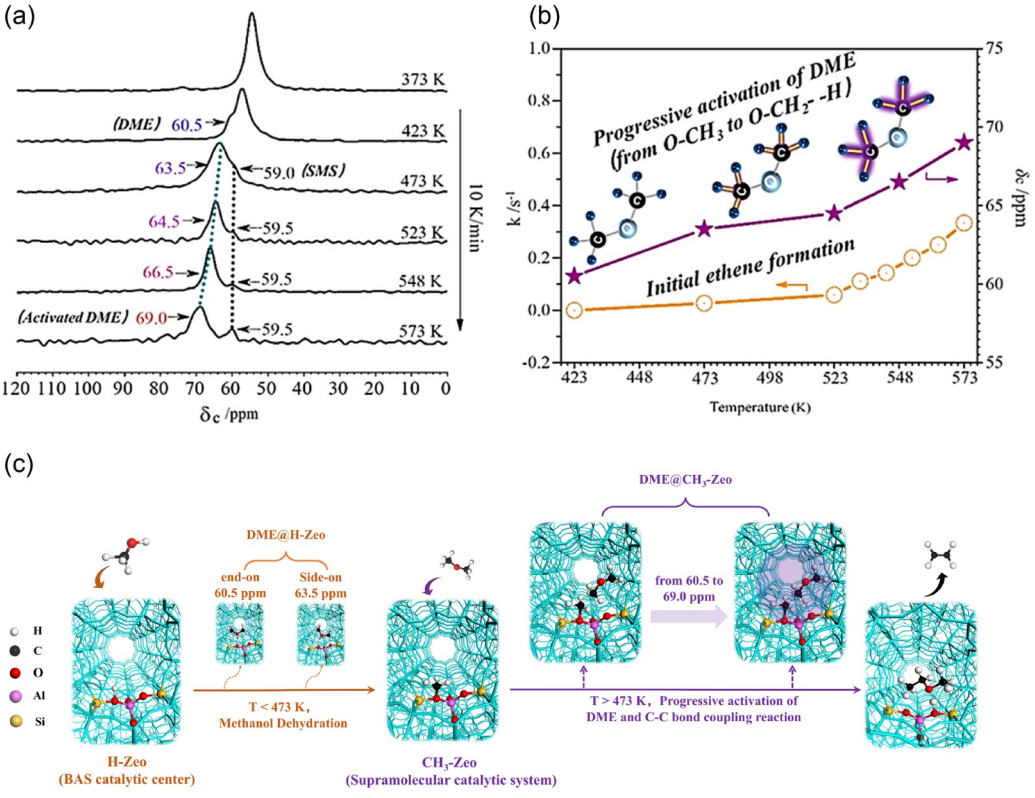

Figure 5 (Color online) The dynamic activation of C1 molecules over HZSM-5 zeolite. (a) *In-situ* ^{13}C MAS NMR spectra during the ^{13}C-methanol continuous-flow conversion at programmed temperatures from 373 to 573 K. (b) The apparent reaction rate of C1 reactants and the chemical shift value of DME as the function of the reaction temperature from 423 to 573 K. (c) Evolution of the catalyst surface during the methanol conversion over HZSM-5 with the temperature variation [39]. Adapted with permission from ref. 39, Copyright 2021 American Chemical Society.

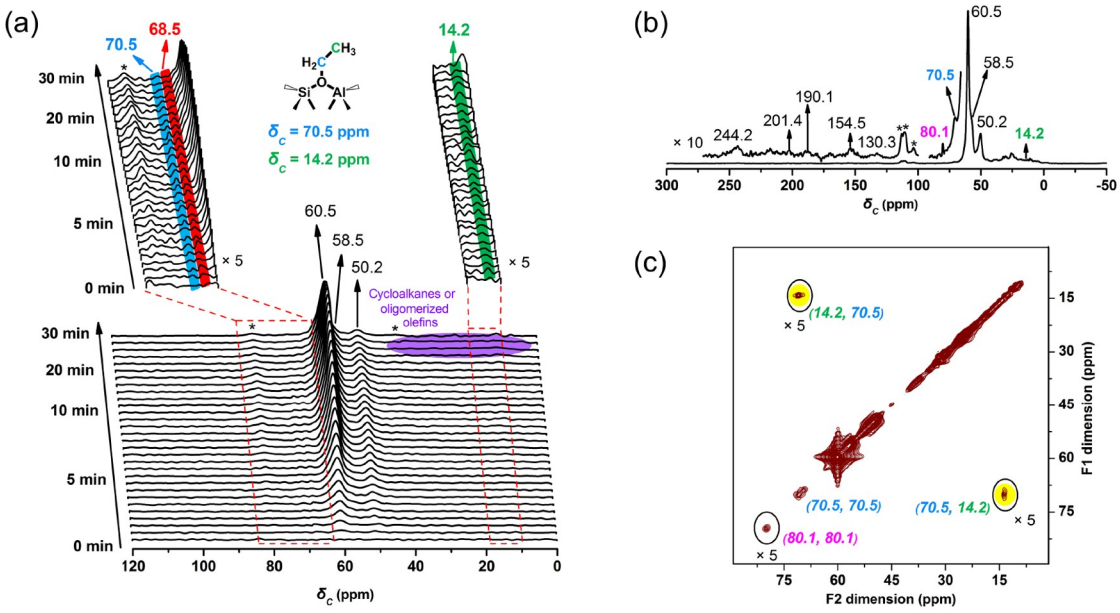

Figure 6 (Color online) *In-situ* solid-state NMR investigations for methanol conversion at the initial MTO reaction stage. (a) *In-situ* solid-state ^{13}C MAS NMR spectra of HSSZ-13 with CF ^{13}C-methanol conversion at 493 K. The spectra were recorded every 30 s from 0 to 10 min and then every 120 s from 10 to 30 min. (b) The ^{13}C CP/MAS NMR spectrum of HSSZ-13 after *in-situ* ^{13}C-methanol conversion at 493 K for 30 min. (c) 2D ^{13}C–^{13}C CORD spin diffusion MAS NMR spectrum of the sample in (b) with a mixing time of 50 ms. The spectra in (b) and (c) were recorded at room temperature. The asterisk symbol (*) indicates the spinning sidebands [37]. Adapted with permission from ref. 37, Copyright 2021 Elsevier B.V.

methylene carbon (70.5 ppm) and the methyl carbon (14.2 ppm) in the 2D ^{13}C–^{13}C combined R2-driven (CORD) spin diffusion MAS NMR spectra (Figure 6c). To explore the complete pathways and dynamic activation/conversion processes of C1 reactants, we further employed an AIMD simulation based on a meta-dynamic method under experimental temperature and pressure. All possible combinations of methanol/DME activation mediated were considered using two collective variables (CVs) by the coordination numbers (CNs) of pivotal bond formation/breakage.

Additionally, we constructed 2D free energy surfaces to visually present the dynamic coupling reactions and the free energy barrier of each pathway (Figure 7a). The evolution of bond distances exhibits the formation/breakage of the typical bonds from C1 species along with simulation time (Figure 7b), visualizing the scene of the dynamic C–C coupling process. These results for such a difficult-to-detect and extremely initial reaction process not only illustrated the dynamic reaction course of C–O and C–H bond breakage and C–C bond formation of C1 species but also shed light on the controversial issue of the first C–C bond formation in MTO reaction.

3.2 Revealing the intermediate role of carbenium ions in the high efficient reaction stage

After the formation of the initial C–C bond via the direct mechanism, the MTO reaction enters the steady-state stage. During this stage, methanol conversion occurs through an efficient indirect "hydrocarbon pool" (HCP) mechanism, which is energetically favorable and can rationally explain the distribution of final products. It has been generally accepted that HCP species, including carbenium ions and their neutral species confined in the zeolite cage or intersection of channels, act as co-catalysts and accelerate the production of hydrocarbons from the C1 reactant [47–49]. However, direct observation of these carbenium ions under *operando* conditions is challenging due to their instability and relatively lower sensitivity of spectroscopy. SsNMR spectroscopy has been proven to be powerful for identifying the structure and behavior of confined intermediates in zeolite catalysts, particularly for cyclic carbenium ions with a characteristic chemical shift larger than 180 ppm. In this section, we summarize the direct capture and observation of HCP species under real working conditions and provide a molecular understanding of these carbenium ions in the MTO process over zeolites.

3.2.1 *The capture and observation of carbenium ions under real MTO conditions*

Carbenium ions are proposed as the important intermediates in the side-chain methylation route and the paring route of the HCP mechanism. With the aid of ssNMR spectroscopy, cyclic carbenium ions represented as heptamethylbenzenium (heptaMB$^+$) and heptamethylcyclopentenyl cations (heptaMCP$^+$) have been verified mostly as intermediates confined within zeolite catalysts. We firstly reported the

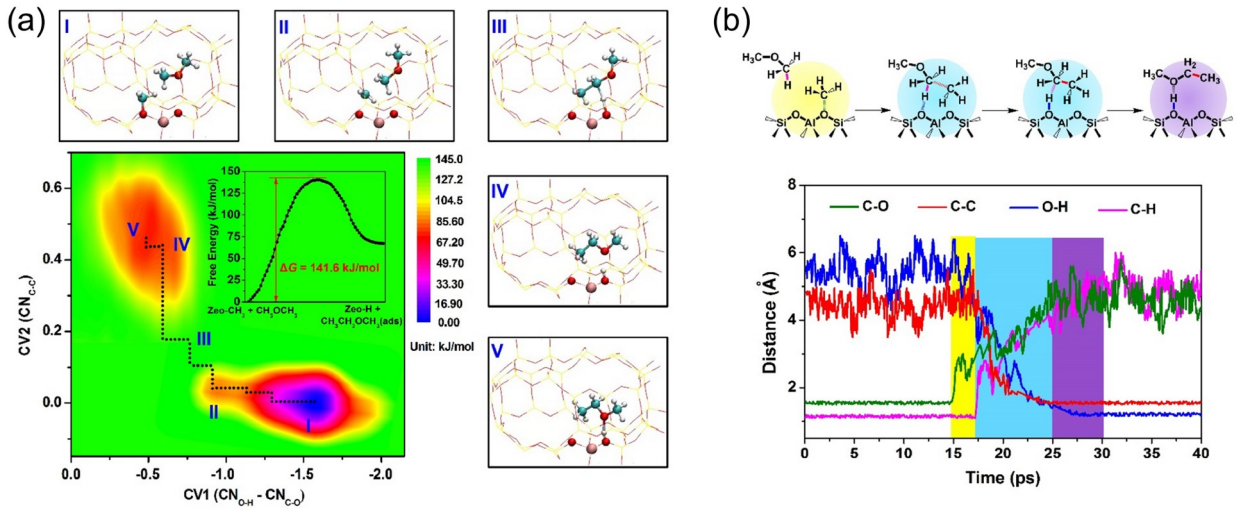

Figure 7 (Color online) AIMD simulation results of the C–C bond formation starting from DME and SMS. (a) 2D free energy surface and minimal energy path of the first C–C bond formation starting from DME and SMS (insets: free energy profiles along with the minimal energy path), where CN_{C-C}, CN_{O-H}, and CN_{C-O} are the coordination numbers of methyl C atoms between DME and SMS, methyl H atom in DME and negatively charged framework O atom, methyl C atom in SMS and its connected framework O atom, respectively. CN_{O-H}–CN_{C-O} is the difference between CN_{O-H} and CN_{C-O}. The snapshots of five representative (meta-) stable states encountered along the reaction trajectory: (I) reactant basin, (II) approaching state, (III) activation state, (IV) product state, and (V) product basin are also shown. The color codes in white, light blue, red, and pink are H, C, O, and Al, respectively. (b) The evolution of the C–O, C–C, O–H, and C–H bond distances in the DME and SMS over HSSZ-13 zeolite with AIMD simulations [37]. Adapted with permission from ref. 37, Copyright 2021 Elsevier B.V.

presence of heptaMB$^+$ on DNL-6 zeolite with large cavities, evidenced by the ^{13}C chemical shifts at 198, 188, and 152 ppm after quenching the conversion of ^{13}C-methanol at 548 K for about 50 min (Figure 8a) [50]. The ^{13}C labeling experiments suggested that olefin formation mainly follows the side-chain mechanism mediated by heptaMB$^+$. Using a similar method, heptaMB$^+$ and pentaMCP$^+$ ions were also directly observed on CHA-type catalysts [51], silicoaluminophosphate (SAPO) molecular sieves [52], and BEA-type zeolites [53] under the real reaction conditions (Figure 8b and 8c). Specifically, the type of carbenium ions observed in ^{13}C NMR experiments was determined by zeolites. For instance, both heptaMB$^+$ and pentaMCP$^+$ have been observed on H-SSZ-13, while only pentaMCP$^+$ was persistent over H-SAPO-34. Based on the proton affinity (PA) calculations of these two carbenium ions, it was found that heptaMB$^+$ should be more stable, which suggested the stability of carbenium ions was not only related to the acid strength of BAS but also to their reactivity during the catalytic transformation.

In addition, the confinement effects of the zeolite channel and cavity also play an important role in the stability of carbenium ions. By carefully analyzing the MTO reaction activity and the retained species over ZSM-22, ZSM-35, and ZSM-5 with 10-membered ring channel systems varying in channel dimensions (Figure 9a), it was found that there is a positive correlation between the MTO reaction activity and the amount of retained organic species in ZSM-22, ZSM-35, and ZSM-5 under the reaction conditions [54]. As shown in Figure 9b, only very weak peaks at 250, 136, and 25 ppm are observed in the ^{13}C MAS NMR spectra of ZSM-22, indicating that little cyclic organic species are retained in the catalyst during the methanol reaction. The intensity of those signals increased slightly on ZSM-35. As for ZSM-5, the signal intensity of aromatics and cyclopentenyl cations is remarkably higher than those on the previous two catalysts. With the aid of GC-MS analysis, we found that the number or size of the alkyl substitution groups of the specific cyclopentenyl cations on ZSM-22 and ZSM-5 is quite different (Figure 9c), suggesting that even a little discrepancy in the channel or channel intersection affects the size and number of substitution groups of these carbenium ions in MTO reaction.

3.2.2 The application of dynamic nuclear polarization (DNP) for the identification of the molecular structure of carbenium ions on catalysts

Although the formation of carbenium ions intermediates has been proved validly on various zeolites, identifying the structure of these carbenium ions remains a significant challenge due to their low concentrations and the intrinsically low sensitivity of NMR when targeting the carbon nuclei with extremely low nature abundance of 1.1%. DNP is a powerful method for significantly improving the sensitivity of ssNMR by multiple orders of magnitude, thereby greatly reducing the acquisition time. We combine ^{13}C isotopic enrichment strategy and efficient DNP MAS NMR to detect the carbenium ions present in low concentrations of 0.002–0.01 mmol g^{-1} [55]. Under microwave irradiation at

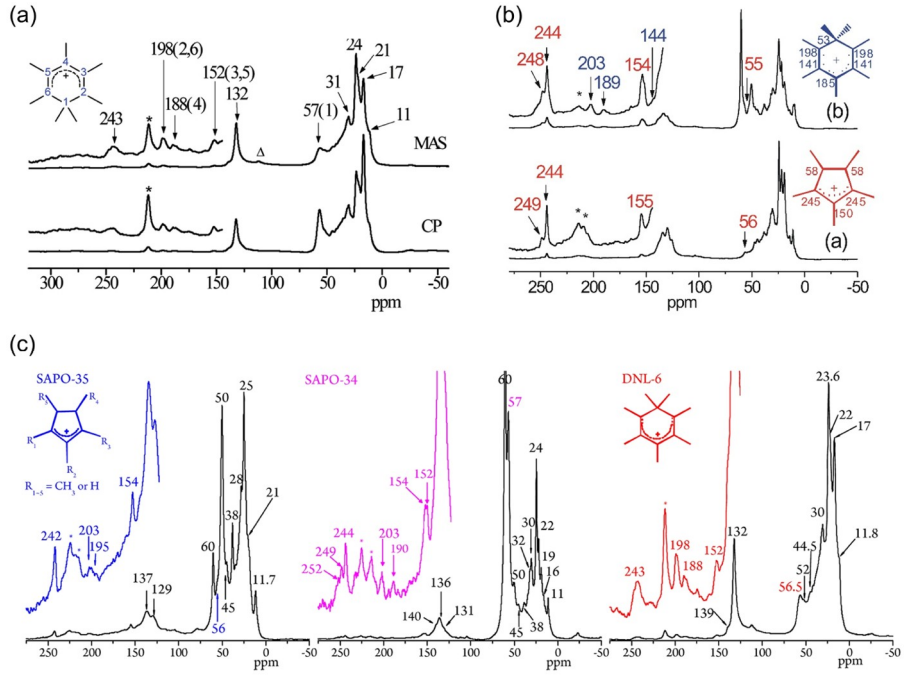

Figure 8 (Color online) The observation of cyclic carbenium ions during MTO reaction on acid zeolites. (a) ^{13}C MAS and CP/MAS NMR spectra of the DNL-6 catalyst after ^{13}C-methanol conversion at 548 K for ~50 min [50]. Adapted with permission from ref. 50, Copyright 2012 American Chemical Society. (b) ^{13}C MAS NMR spectra of a) retained organic species in HSAPO-34 after continuous-flow $^{13}CH_3OH$ reaction at 573 K for 15 min and b) retained organic species in H-SSZ-13 after continuous-flow $^{13}CH_3OH$ reaction at 548 K for 25 min. Insets: calculated ^{13}C chemical shifts of pentaMCP$^+$ and heptaMB$^+$ ions inside the H-SSZ-13 zeolite [51]. Adapted with permission from ref. 51, Copyright 2013 Wiley-VCH GmbH. (c) ^{13}C MAS NMR spectra of the catalysts after ^{13}C-methanol conversion for ~50 min at 548 K for DNL-6 and high-silica SAPO-34, and 30 min at 573 K for SAPO-35 [52]. Adapted with permission from ref. 52, Copyright 2014 American Chemical Society. The asterisk denotes spinning side-bands.

9.4 T, the ^{13}C CP MAS NMR spectra can be recorded within minutes. The typical signals of carbocations (150–250 ppm) were observed on both zeolites in DNP-enhanced ^{13}C CP MAS NMR spectra, with the ^{13}C signal enhancements $\varepsilon_{C\ CP}$ as 10 and 40 for M-β and MMM-β, respectively (Figure 10). This enhancement enables the 2D ^{13}C–^{13}C refocused INADEQUATE (Incredible Natural Abundance DoublEQUAntum Transfer Experiment), which usually otherwise takes days or even weeks without DNP. By analyzing the through bond correlations as shown in Figure 11, the structures of trimethylcyclopentenyl cation, heptamethylbenzenium cation, dimethylcyclohexenyl cation, and methylnaphthalenium ions were successfully distinguished. This is the first case for the application of DNP to the mechanism investigation of highly reactive intermediates in heterogeneous catalysis.

3.2.3 The role of carbenium ions: from dual cycle to triple cycle mechanism in highly efficient stage

The next remaining issue is whether the carbenium ions are active intermediates rather than spectators. Based on the aforementioned great progress in the observation and identification of the carbenium ions confined in zeolites characterized by *in-situ* ^{13}C ssNMR in sections 3.2.2 and 3.2.1, we clarified the crucial role of carbenium ions in MTO reaction by combining ^{13}C ssNMR with complementary $^{12}C/^{13}C$-methanol switch experiments. These findings led us to propose a hypercycle reaction network constructed by the dynamic alternation/interweaving of the catalytic cycles.

Determined by quantitatively calculating the integral area of the characteristic peaks for the ring carbon atoms, the concentration evolutions of heptaMB$^+$ and pentaMCP$^+$ showed the same trend with methanol conversion on SSZ-13 [51]. This close correlation between the concentrations of two kinds of carbenium ions and methanol conversion indicated that heptaMB$^+$ and pentaMCP$^+$ might participate in both paring and side-chain methylation mechanisms. This assumption was confirmed by $^{12}C/^{13}C$-methanol switch experiments with the aid of GC-MS. When ^{13}C-methanol was introduced to H-SSZ-13 catalyst with confined ^{12}C pentaMCP$^+$, the isotopic distribution of pentaMCP (the deprotonated counterpart of pentaMCP$^+$) indicated that ^{13}C atoms are incorporated into pentaMCP$^+$ and olefin products during the MTO reaction. Based on these observations, we proposed a pathway following the paring mechanism and side-chain methylation mechanism with heptaMB$^+$ and pentaMCP$^+$ as key intermediates (Figure 12a). These two reaction cycles were demonstrated to be energetically feasible, but the side-chain methylation mechanism is the more predominant pathway on H-SSZ-13 zeolite.

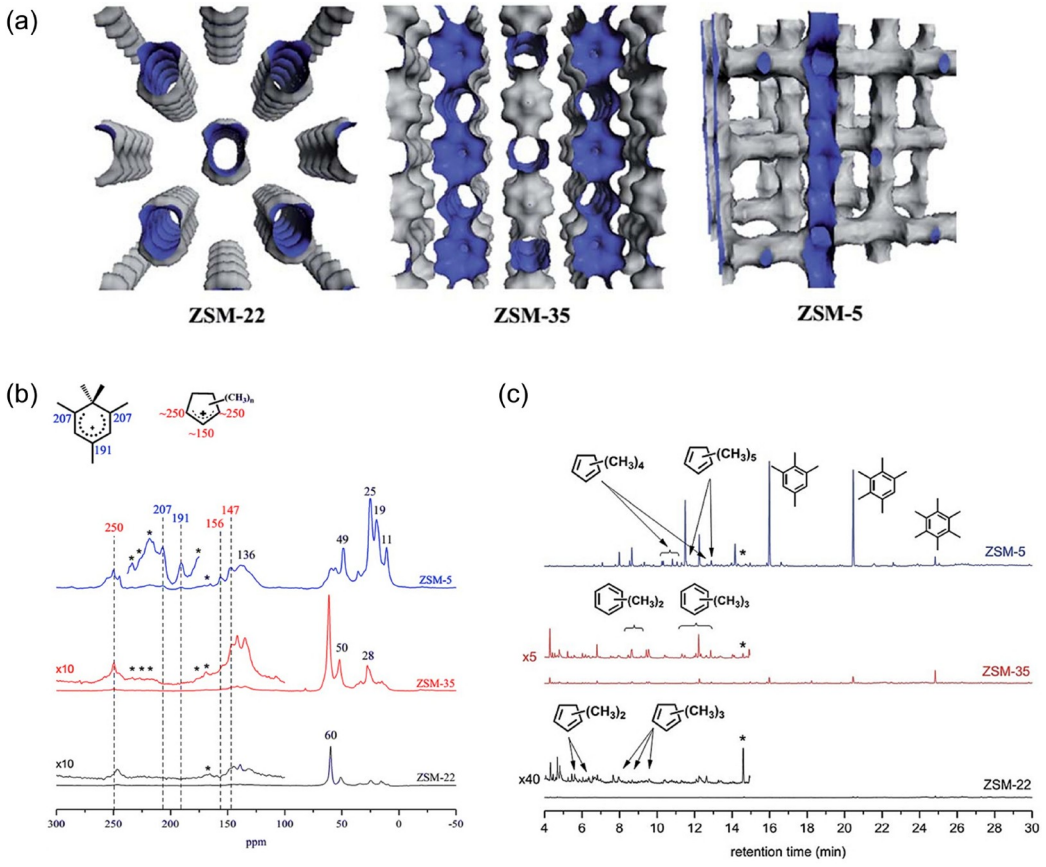

Figure 9 (Color online) (a) Illustrations of the channel systems of ZSM-22, ZSM-35 and ZSM-5. (b) ^{13}C MAS NMR spectra of retained species at the respective highest conversions over three zeolites at the reaction temperature of 573 K and methanol WHSV of 2 h^{-1}. (c) The chromatographic analysis of the three samples, * denotes internal standard C_2Cl_6 [54]. Adapted with permission from ref. 54, Copyright 2016 Royal Society of Chemistry.

In the dual-cycle mechanism, the two cycles are interconnected through the hydrogen transfer reaction. Subsequently, we reported that the balance of these two catalytic cycles can be adjusted by varying the catalyst-methanol contact times of MTO reactions [56]. This adjustment can be achieved by varying the weight hourly space velocity (WHSV) values of methanol conversion at 573 K over HZSM-5, which correspond to different contact times of 156, 32, and 16 ms for WHSV values of 2, 6, and 12 h^{-1}, respectively. The analysis of reaction effluents and confined organics indicated that a longer contact time, achieved by using lower WHSV values, promoted the hydrogen transfer of alkene products, thus leading to an increase in the aromatic cycle to promote the generation and accumulation of retained organic species. On the contrary, the reduction in contact times lessened the extent of the hydrogen transfer reaction and further suppressed the aromatic cycle to push the alkene cycle to become the dominant route during the MTO reaction. These findings provide an effective strategy for manipulating the MTO reaction to generate target products over the ZSM-5 catalyst.

With a deep understanding of the indirect mechanism, we established a novel cyclopentadienes-based cycle in which light olefins were formed with methylcyclopentadienes as critical intermediates on the H-SAPO-34 catalyst (Figure 12b) [57]. By *in-situ* ^{13}C MAS NMR, the methylcyclopentenyl cations and their deprotonated counterparts (methylcyclopentadienes, MCP) were validated on H-SAPO-34 by the appearance of a group of peaks at 56, 154, 245 ppm, and the characteristic signal at 135 ppm, respectively. Additionally, the corresponding neutral species were analyzed by GC-MS, further confirming the presence of these species. Subsequently, the reactivity of these retained species was evaluated in $^{12}C/^{13}C$-methanol switch experiments and DFT theoretical calculations. Our findings indicated that MCP species were critical intermediates in the methylation steps. Based on these results, we proposed a cyclopentadienes-based catalytic cycle, which acts as a bridge linking the traditional alkenes-based and aromatics-based cycle. Recently, we verified that this cyclopentadienes-based cycle is an energetically feasible route for ethene formation in an H-RUB-50 catalyst with a small cavity [58]. These results further highlighted the influences of steric constraint and the host–guest interaction induced by the cavity structure of zeolites on the formation of intermediates and reaction pathways.

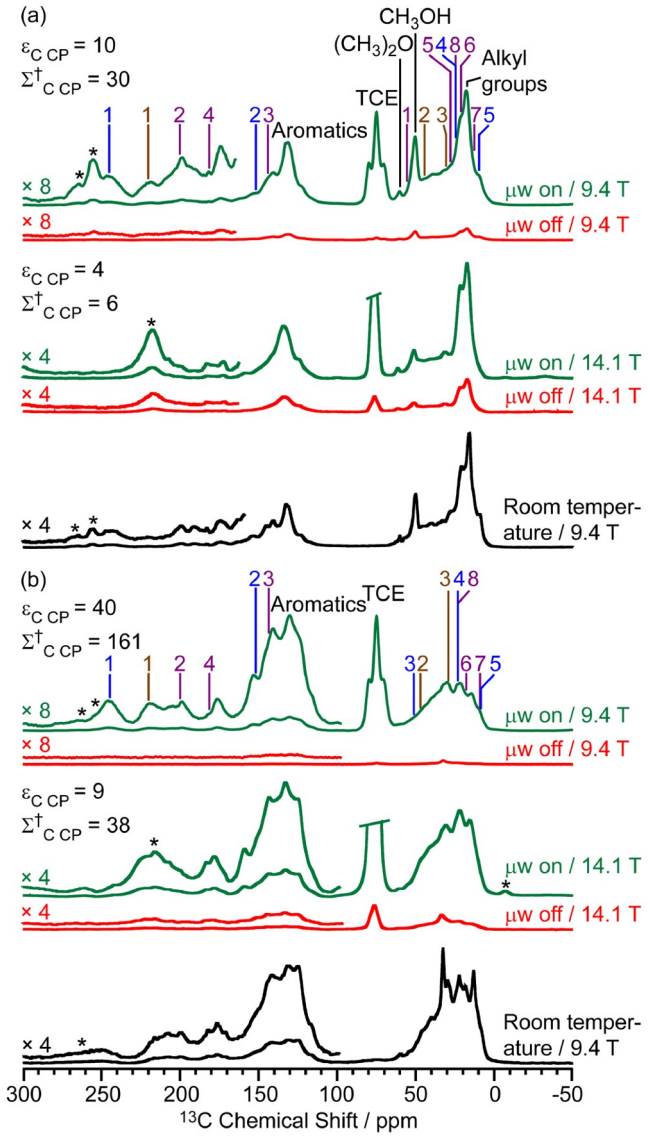

Figure 10 (Color online) ^{13}C CP MAS DNP spectra at 9.4 T, 110 K and 14.1 T, 125 K and room temperature experiments at 9.4 T of (a) activated M-β and (b) activated MMM-β. The experimental times for the spectra of activated M-β are ~7 min at 9.4 T DNP, ~9 min at 14.1 T DNP and ~52 min at room temperature at 9.4 T without DNP while for activated MMM-β they are ~2 min at 9.4 T DNP, ~6 min at 14.1 T DNP and ~1,036 min at room temperature at 9.4 T without DNP. Σ† refers to the overall DNP gain and is calculated by comparing the DNP data to room temperature 9.4 T NMR spectra. All spectra were recorded at a MAS rate of 12.5 kHz with asterisks (*) denoting spinning sidebands. M-β: microporous zeolite with pore size <1 nm; MMM-β: micro–meso–macroporous zeolite with mesopore and macropore sizes of 2.5–4.0 and 100–300 nm [55]. Adapted with permission from ref. 55, Copyright 2018 Royal Society of Chemistry.

3.2.4 The role of carbenium ions: Linking the initial stage and the highly efficient stage

Along with the initial C–C formation in the initial stage, the accumulation of initial olefins and HCP species in the transition stage promotes the reaction into a highly efficient steady-stage governed by the HCP mechanism. Understanding the formation and evolution of initial hydrocarbon pool species is very important to draw a complete interlaced hypercycle reaction network. With the aid of *in-situ* ^{13}C MAS NMR spectroscopy under the *operando* condition, we found the appearance of MCP^+ with the characteristic signals at 245 and 154 ppm and polymethylbenzenes (PMBs) with the signal at 131 ppm during the transition stage of the MTO reaction over H-SSZ-13 catalyst at 548 K (Figure 13a) [59]. Notably, MCP^+ was formed earlier compared with PMBs, according to the chronological order of ^{13}C MAS NMR signal occurrence. This phenomenon is consistent with our previous *ex-situ* studies of the MTO reaction on H-SSZ-13 [51]. These two unsaturated species gradually accumulated during this transition stage. Then, we confirmed the formation of MCP^+ from ethene accompanied by the formation of aromatic species (130 ppm) and oligomers of ethene (0–50 ppm), indicating that the initial MCP^+ and MCP species can be formed via a series of reactions, such as oligomerization, cyclization, and hydrogen transfer of initial olefins (Figure 13b). Combined with DFT theoretical calculations, it was demonstrated that the formations of initial PMBs at the initial stage originate from MCP^+ with methanol reaction via the deprotonation, hydride-transfer reactions, and ring expansion. Furthermore, by analyzing the ^{13}C-isotope distribution of the organic species during the co-reaction of ^{12}C-pentaMCP and $^{13}CH_3OH$ (Figure 13c), we confirmed that PMBs can be directly generated from MCP^+ through reactions with methanol. This work reveals the important role of MCP^+ and establishes a bridge between the initial stage and the efficient steady-stage of the reaction (Scheme 2).

3.3 Elucidation of the deactivation mode in the deactivation stage

Catalyst deactivation is a crucial obstacle for improving catalytic performance. In the steady state, the continuous accumulation and growth of HCP species can be gradually accumulated on the surface or pores of zeolites, leading to the formation of heavier carbonaceous deposits, known as "coke" [11,60]. These cock species gradually blocked the pores of zeolites, and then reduced the diffusion efficiency of reactants, and the number of available active centers, ultimately leading to the obstruction of the methanol reaction and catalyst deactivation [61]. It is worth noting that the mechanism of catalyst deactivation is influenced by multiple factors, such as the inherent topological structure and acidic property of zeolites, and operating conditions. Therefore, the in-depth analysis of the spatial distribution of coke species and their potential impact on quality transfer and catalyst acidity is of great importance for further optimization of MTO processes and improvement of catalyst performance.

(HP) ^{129}Xe NMR spectroscopy is a universal technique for probing the internal pore structure and different local che-

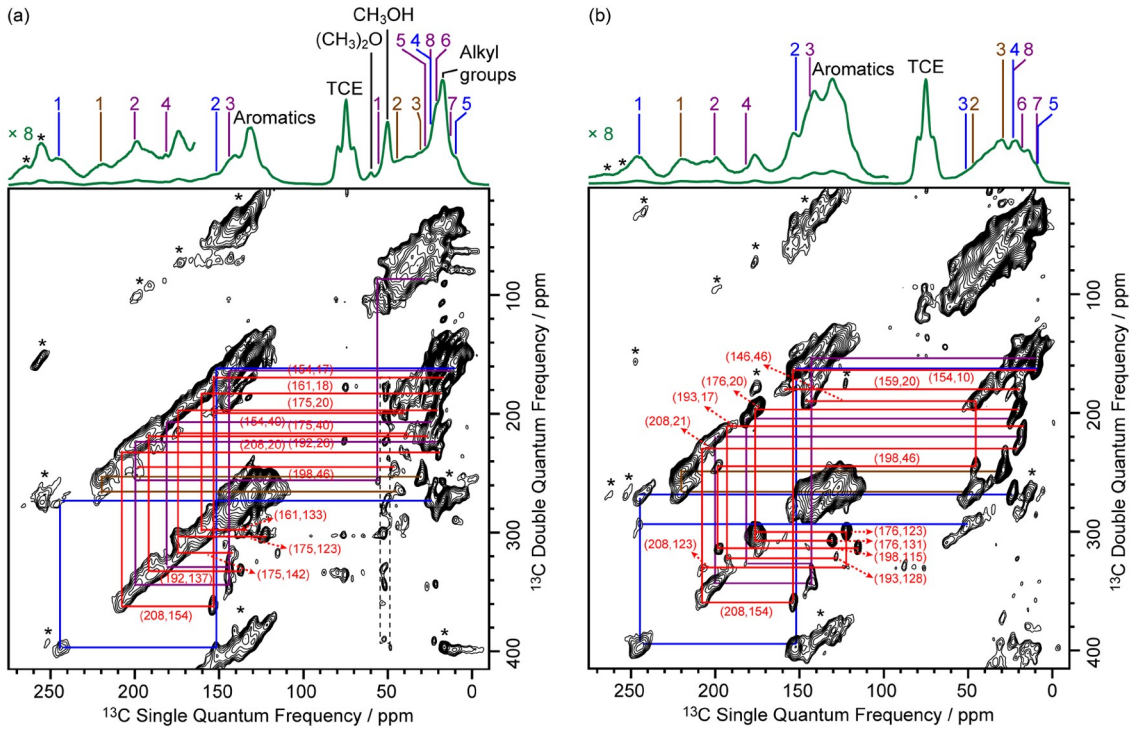

Figure 11 (Color online) DNP enhanced 2D ^{13}C–^{13}C refocused INADEQUATE spectra of (a) activated M-β and (b) activated MMM-β. Data were recorded at B_0 = 9.4 T and a MAS frequency of ν_r = 12.5 kHz. Experimental times for (a) and (b) are 20 and 14 h, respectively. Signals in the black dashed box in (a) correspond to t_1 noise. Asterisks denote spinning sidebands [55]. Adapted with permission from ref. 55, Copyright 2018 Royal Society of Chemistry.

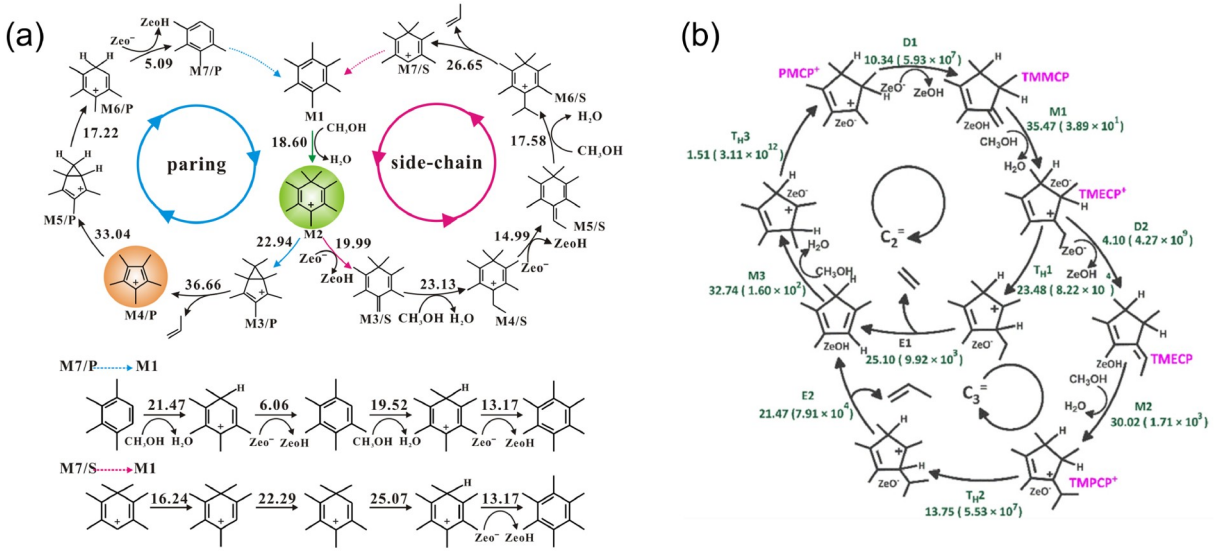

Figure 12 (Color online) (a) Catalytic cycles of the paring and side-chain reaction mechanisms for the MTO conversion with the involvement of pentaMCP$^+$ and heptaMB$^+$ in H-SSZ-13 zeolite. The calculated energy barriers are given in kcal mol^{-1} [51]. Adapted with permission from ref. 51, Copyright 2013 Wiley-VCH GmbH. (b) Mechanism routes based on the proposed cyclopentadienes-based cycle for ethene and propene formation over H-SAPO-34 [57]. Adapted with permission from ref. 58, Copyright 2019 American Chemical Society.

mical environments of porous materials [62]. Recently we applied the temperature-variation HP ^{129}Xe NMR spectroscopy to investigate the heterogeneity of the porosity in the SAPO-34 catalysts with coke deposition during the MTO reaction [63]. As shown in Figure 14a, xenon in the gaseous phase (represented as a narrow peak at 0 ppm) and xenon adsorbed in CHA nanocages (represented as a broad peak at higher chemical shift) can be distinguished. The chemical shift of adsorbed xenon increased from 84 ppm to 134 ppm on fresh SAPO-34 due to strong Xe–Xe interaction when the

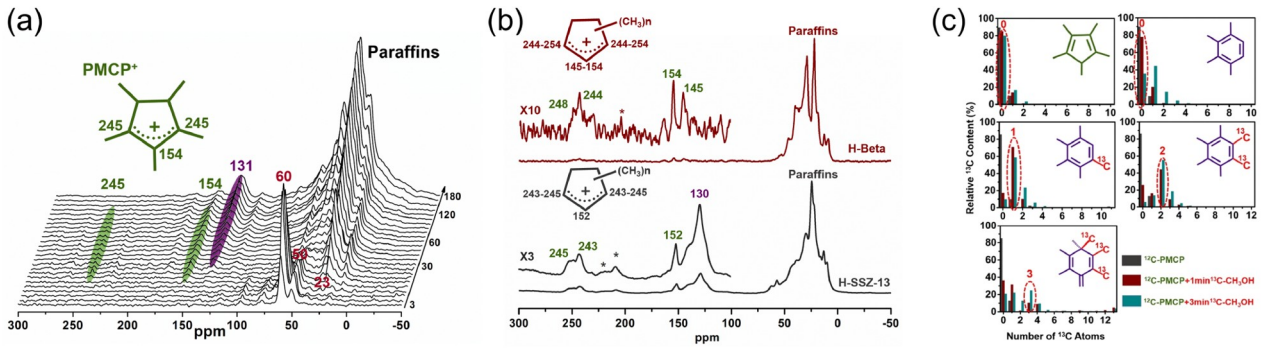

Figure 13 (Color online) (a) *In-situ* ^{13}C MAS NMR spectra of $^{13}CH_3OH$ reaction over HSSZ-13 catalyst at 548 K with methanol WHSV of 1.0 h^{-1}. (b) ^{13}C MAS NMR spectra of H-SSZ-13 and H-Beta zeolites on the reaction of adsorbed ^{13}C-ethene at 548 K for 60 and 30 s, respectively. Asterisk denotes spinning sideband. (c) The isotopic distribution the organic species retained in H-Beta catalyst after the co-reaction of ^{12}C-pentaMCP and $^{13}CH_3OH$ at 275 °C for 1 min (red line or column) and 3 min (blue line or column); the black line or column is the control experiment of ^{12}C-pentaMCP reaction for 1 min [59]. Adapted with permission from ref. 59, Copyright 2020 American Chemical Society.

temperature decreased from 293 to 193 K. However, the chemical shift of adsorbed xenon remains unchanged on spent catalysts, while the signal intensities of adsorbed xenon decreased obviously along with the extension of reaction time. Moreover, the variation of the relative intensity of adsorbed xenon at 293 K with the coke amount in SAPO-34 catalysts did not follow a linear relationship. These observations revealed a non-uniform spatial distribution of coke in SAPO-34 crystals, which was supported by the confocal fluorescence microscopy (CFM) techniques (Figure 14b).

Since the first application of the pulsed field gradient (PFG) NMR in 1965 [64], this technique has evolved into an essential tool for studying the diffusion characteristics and motion of molecules within porous materials [65,66]. Utilizing pulsed field gradients, this technique tracks spatial displacements and monitors the movement of adsorbed guest molecules within materials [67]. The diffusion data are obtained using a PFG pulse sequence, employing either a spin-echo (SE) or a stimulated-echo (STE) method. In PFG NMR

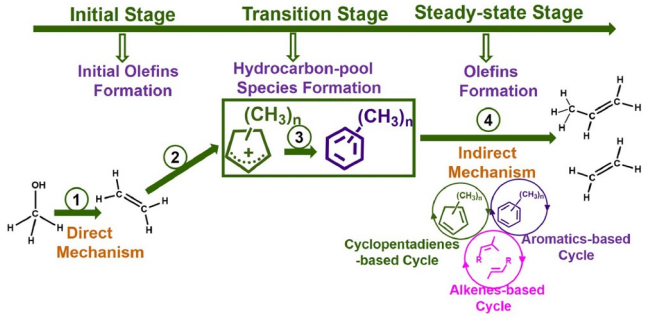

Scheme 2 (Color online) Whole mechanism of MTO reaction. (1) The initial ethene is generated from methanol by direct mechanism; (2) MCP species are produced from initial ethene; (3) PMBs species are produced from the co-reaction of MCP species and methanol; (4) the olefins are formed via indirect mechanism including of aromatics-based, alkenes-based, and cyclopentadienes based cycles [59]. Adapted with permission from ref. 59, Copyright 2020 American Chemical Society.

experiments, the diffusion coefficient is accurately estimated by varying the intensity of the pulsed gradients, which induces exponential signal attenuation. Therefore, PFG NMR provides insights on the average mass transfer behavior of guest molecules within the crystal, with spatial and temporal resolution on the order of micrometers and milliseconds, respectively. To clarify the effect of coke species trapped inside SAPO-34 catalysts on mass transport, ^{1}H pulsed field gradient (PFG) NMR spectroscopy was employed to evaluate the quantitative variation of mass transport within a 7–10 μm SAPO-34 crystal with coke deposition from the microscopic perspective [63]. Methane and ethene with small kinetic diameters of ca. 3.8 and 3.9 Å were used as probe molecules. The self-diffusion coefficients of these adsorbed molecules can be obtained from a stimulated echo sequence with bipolar-gradient (13-interval sequence, PGSTEBP) according to the Stejskal–Tanner equation (1).

$$I(g) = I(0)\exp\left[-(\gamma\delta g)^2 D\left(\Delta - \frac{\delta}{3}\right)\right] \quad (1)$$

where $I(0)$ and $I(g)$ represent the signal amplitude using $g = 0$ and variable g, respectively. In this equation, γ stands for the gyromagnetic ratio, δ is the effective gradient pulse duration, g is gradient strength, Δ denotes the diffusion time, and D represents the self-diffusion coefficient. Additionally, the apparent intracrystalline diffusion activation energies (E_a) of the adsorbate in the fresh and spent catalysts were calculated based on the Arrhenius law (2).

$$D = D_0\exp(-E_a / RT) \quad (2)$$

As shown in Figure 14c, a decrease in the diffusion coefficient of methane was observed from 4.11×10^{-11} m^2 s^{-1} for fresh catalyst to 2.71×10^{-11} m^2 s^{-1} in the early stage within 18 min. This decrease was due to the formation of benzene and methyl naphthalene in the catalyst. As the reaction prolongs, the formation of coke leads to a sharp drop in the diffusion coefficient. The diffusion coefficient of ethylene is

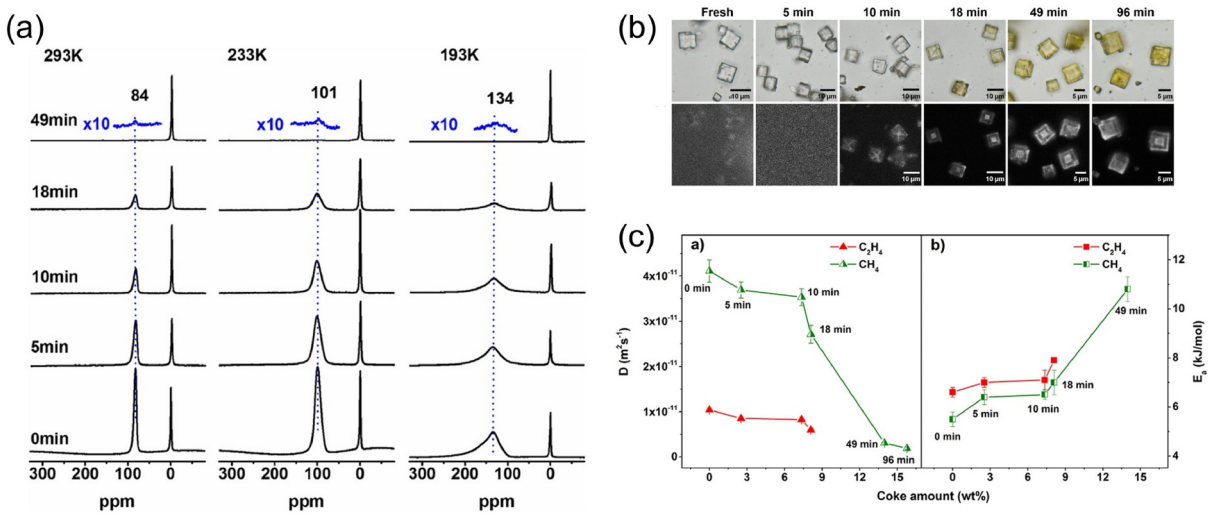

Figure 14 (Color online) (a) Temperature-dependent HP ^{129}Xe NMR spectra of xenon adsorbed in fresh and spent SAPO-34 catalysts after the MTO reaction at 673 K for various reaction times. (b) a) Brightfield images and b) confocal fluorescence microscopy images of SAPO-34 crystals after MTO conversion at 673 K for various reaction times. Fluorescence from the interior of the crystal. (c) The diffusion performance of the SAPO-34 catalyst. a) The variation in intracrystalline self-diffusion coefficients of CH_4 and C_2H_4 at 298 K and b) diffusion activation energies determined in the temperature range 298–328 K in fresh and spent SAPO-34 as a function of coke amount. A loading of 0.5 molecules per cage is used [63]. Adapted with permission from ref. 63, Copyright 2018 Elsevier B.V.

much lower than that of methane owing to its larger molecular size, resulting in a stronger diffusion limitation effect on ethene. Correspondingly, the apparent intracrystalline diffusion activation energies of methane and ethene exhibit a growing trend, corresponding to the variation of the diffusion coefficient. Therefore, the main causes for intracrystalline diffusion limitation in the MTO reaction over SAPO-34 are coke formation and deposition, which modify pores or cavities of zeolites. In a heavily deactivated catalyst, pore blockage and cavity occupation become significant, greatly restricting the mass transport of reactants and products.

4 Understanding the host-guest interaction during MTO reaction

4.1 The host–guest interaction between reactants and zeolites

We developed a combined approach of *in-situ* continuous-flow HP ^{129}Xe MAS NMR coupled with ^{13}C MAS NMR to study the adsorption and reaction kinetics in CHA nanocages [25]. Xenon atoms possess a large spherical electron cloud which is highly sensitive to the surrounding environment. Any small changes in the structure, composition, and pore channels of zeolites after the adsorption will impact the electron cloud density, leading to the migration of chemical shifts in xenon. Thus, the kinetic and dynamic processes of methanol adsorption and reaction in CHA nanocages can be monitored by one- and two-dimensional HP ^{129}Xe MAS NMR spectroscopy under CF conditions [25]. Our results, as shown in Figure 15, reveal that the chemical shift of ^{129}Xe confined in empty cages is 84 ppm. Subsequent injection of ^{13}C-methanol led to the appearance of two new signals at 92 and 88 ppm, attributed to "adsorption zone" and "reaction zone" in the CHA cages, respectively. These findings were in accordance with the evolution of ^{13}C signals observed from *in-situ* ^{13}C MAS NMR spectra. Furthermore, the kinetic and dynamic processes of methanol adsorption and reaction in CHA nanocages have been successfully monitored by one- and two-dimensional HP ^{129}Xe MAS NMR spectroscopy. This allowed us to determine the quantitatively kinetic curves and apparent activation energy of the nanocages involving the active site.

4.2 The host–guest interaction between HCP species and zeolites

The HCP species has been recognized as the species confined in the cavity of channel intersection of zeolites, indicating a strong host–guest interaction between these intermediates and the zeolite structure. However, characterizing the host-guest interaction in this organic-inorganic hybridized system is extremely time-consuming due to the limited sensitivity of ^{13}C in carbenium ions and ^{29}Si in the zeolite framework. With the DNP enhanced ssNMR, the host–guest interaction between different silicon sites of zeolites and hydrocarbon pool species can be quantitatively determined. For instance, ^{29}Si–^{13}C REDOR experiments reintroduce the ^{29}Si–^{13}C dipolar couplings under MAS to quantitatively explore the spatial proximities between the confined carbon species and surface sites of the zeolite

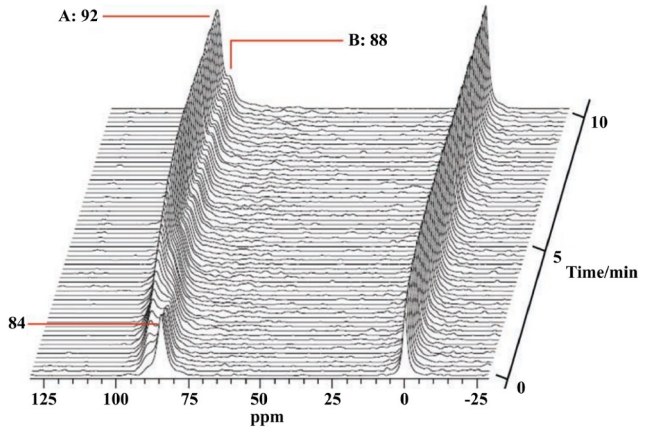

Figure 15 (Color online) *In-situ* HP ^{129}Xe MAS NMR spectra recorded with time resolution of 10 s per spectrum as a function of time during reaction of methanol in CHA nanocages at 453 K [25]. Adapted with permission from ref. 25, Copyright 2009 American Chemical Society.

(Figure 16a) [55]. The REDOR curves of M-β for different Si sites (Figure 16b) demonstrated that both Q4 and Si(1Al) sites have the strongest interaction with the hydrocarbon pool species in activated M-β. This suggested that van der Waals interaction with the zeolite framework dominates the adsorption of these hydrocarbon pool species within the micropores.

4.3 The host–guest interaction in water-induced structural dynamic process

Water is produced as a byproduct of methanol dehydration in the induction period, which is an inevitable step in the activation of methanol. In industrial processes, co-feeding water helps regulate the heat balance by lowering the partial pressure of the reactants and removing heat from the reactor. Additionally, water reduces the catalyst coking by competing with reactants for access to the active sites, thereby slowing down the reaction. Therefore, zeolites and SAPO molecular sieves typically work in a water vapor atmosphere at elevated temperatures.

Generally, the frameworks of zeolites/SAPO catalysts are considered hydrothermally stable under hydrothermal conditions, retaining their crystallinity and acidity even in hydrothermal environments. Using ^{17}O MAS NMR, the interaction of $H_2{}^{17}O$ with SAPO-34 molecular sieve was successfully revealed under mild hydrothermal conditions [68]. After steaming SAPO-34 with $H_2{}^{17}O$ at 373, 473, and 573 K, two broad resonances at 21 and 48 ppm appeared in the ^{17}O MAS NMR (Figure 17a). The multiple-quantum (MQ) MAS NMR technique is able to significantly increase the spectra resolution and obtain the isotropic spectra in the indirect dimension. By employing the 2D ^{17}O MQ MAS NMR spectrum (Figure 17b), these signals were attributed to the framework ^{17}O atoms in the Si–O–Al and P–O–Al species, respectively, indicating the incorporation of ^{17}O atoms in $H_2{}^{17}O$ into SAPO-34 framework. During this water-induced structural dynamic process, the amount of acid sites remains unchanged, as confirmed by quantitative analysis of ^{1}H MAS NMR spectra (Figure 17c). Notably, *in-situ* ssNMR characterization of this dynamic process has failed, suggesting that this dynamic and reversible process is very fast and beyond the time resolution of *in-situ* NMR techniques. Therefore, we confirmed the tetrahedrally coordinated structure of SAPO-34 undergoes a dynamic T–O–T bond breaking by the hydrolysis (Figure 17d).

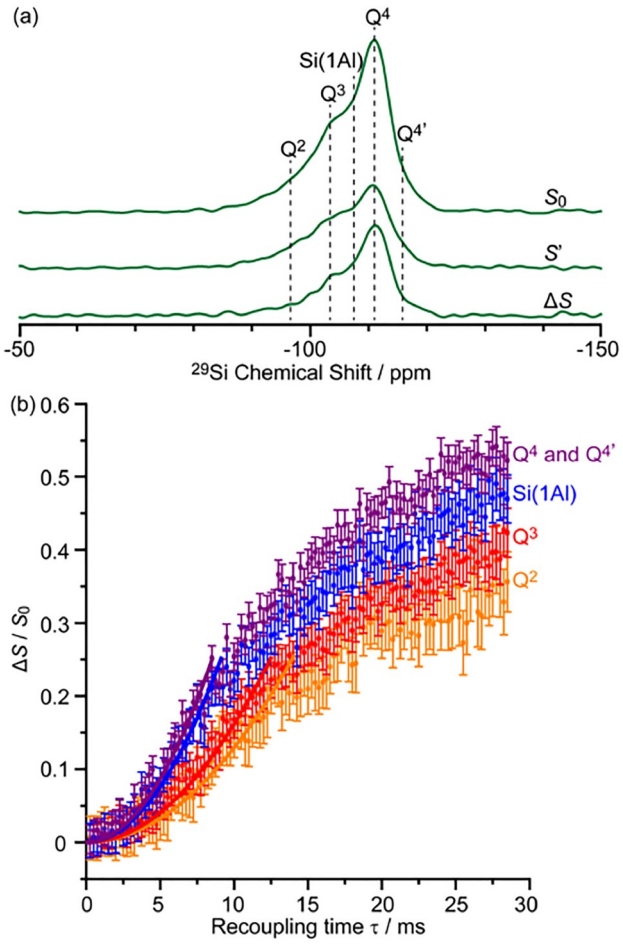

Figure 16 (Color online) DNP enhanced ^{29}Si CP spin echo spectrum (S_0) and ^{29}Si REDOR spectrum (S') with the reintroduction of dipolar couplings at a recoupling time of 28.5 ms. ΔS is the difference spectrum S_0–S'. Spectra were recorded at 9.4 T on activated M-β. (b) ^{29}Si REDOR fraction $\Delta S/S_0$ as a function of the recoupling time up to 28.5 ms. M-β: microporous zeolite with pore size < 1 nm; MMM-β: micro–meso–macroporous mesopore zeolite with macropore sizes of 2.5–4.0 and 100–300 nm [55]. Adapted with permission from ref. 55, Copyright 2018 Royal Society of Chemistry.

Furthermore, in the hydrothermal conditions, the bulky basic molecules of pyridine and trimethylphosphine (TMP) were successfully encapsulated into the CHA cavities of SAPO-34. Notably, the diameters of pyridine (5.3 Å) and TMP (5.5 Å) are much larger than the 8-MR pore sizes of

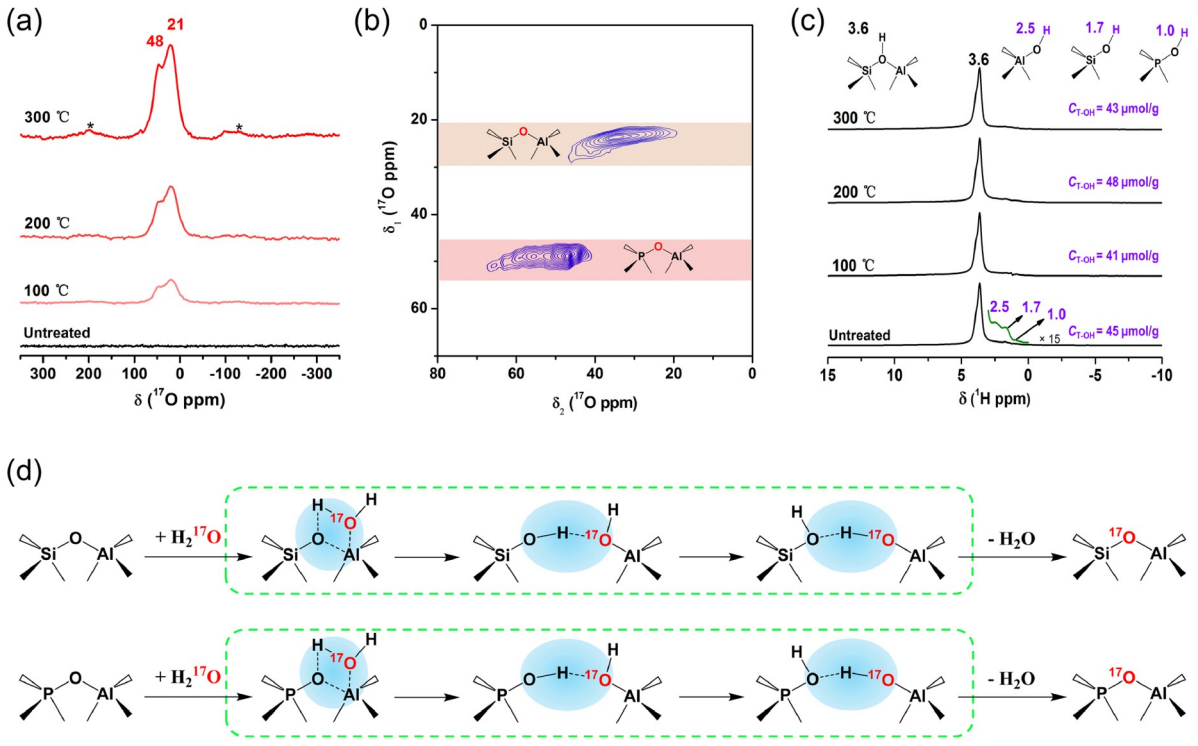

Figure 17 (Color online) (a) The ^{17}O MAS NMR spectra of $H_2{}^{17}O$ steamed SAPO-34 at 373, 473, and 573 K, and the untreated sample for comparison. (b) The 2D ^{17}O MQMAS NMR spectrum of $H_2{}^{17}O$ treated SAPO-34 at 573 K. (c) The ^{1}H MAS NMR spectra of $H_2{}^{17}O$ treated SAPO-34 at 373, 473, and 573 K, and the untreated sample for comparison. T–OH presents the terminal hydroxyl groups Al–OH, Si–OH, and P–OH. (d) Schematic illustration of the proposed route for ^{17}O incorporation from $H_2{}^{17}O$ into the Si–O–Al (top) and P–O–Al (bottom) species and the substitution of original framework O atoms of molecular-sieve framework through reversible breaking and forming of T–O–T bonds. All the spectra in (a–c) were performed on a 4 mm H–X–Y triple resonance probe at room temperature. Prior to NMR spectroscopy, all the $H_2{}^{17}O$ steamed samples and untreated samples were dehydrated at 573 K for 2 h under vacuum. The asterisk indicates spinning sidebands [68]. Adapted with permission from ref. 68, Copyright 2020 Wiley-VCH GmbH.

SAPO-34 (3.8 Å × 3.8 Å). The successful accommodation of TMP and pyridine in CHA cavities of SAPO-34 was confirmed by ^{31}P and ^{1}H MAS NMR spectroscopy. Through 2D ^{1}H–^{31}P HETeronuclear CORrelation (HETCOR) NMR spectroscopy, we analyzed the interactions between TMP and the acid sites and identified four different Brønsted acid sites in SAPO-34 (Figure 18a and 18b). Additionally, this extraordinary introduction of bulky molecules into the CHA cavities of SAPO-34 significantly improved the catalytic performances in MTO reaction. The modified SAPO-34 catalysts exhibited excellent selectivity for low-carbon olefins in MTO reaction, especially with a significant increase in ethylene selectivity by more than 22% during the initial period of MTO reaction (Figure 18c). These findings not only reveal the dynamic and reversible T–O–T bonds breaking and forming process of the molecular sieves under the hydrothermal environment, but also provide an effective approach with great potential for wider range of applications.

5 Summary and outlook

In conclusion, ssNMR spectroscopy has emerged as one of the most important methods for unraveling the complex mechanisms and exploring the host–guest interactions under the real MTO reaction condition. By observing and tracking true reactive intermediates identified through *in-situ* ssNMR spectroscopy, we have established a comprehensive dynamic route that includes the adsorption and activation of reactants, the continuous formation of the initial C–C bond from activated C1 intermediates, the transformation of the initial alkene to highly reactive HCP species, and the efficient generation of products from these HCP species. The combination of *in-situ* techniques with 2D correlation spectra has successfully elucidated the host–guest interactions during the MTO process. These breakthroughs have provided valuable guidance for optimizing the catalysts in industry processes.

Despite the unprecedented progress driven by the application of ssNMR in the MTO process, there remain numerous captivating opportunities for further exploration and advancement. On one hand, the development of *in-situ* ssNMR techniques with high sensitivity and resolution under harsh real working conditions is still incipient. We anticipate the design and development of *in-situ* techniques that can operate under high pressure and high temperature in continuous-flow conditions. On the other hand, the collaboration

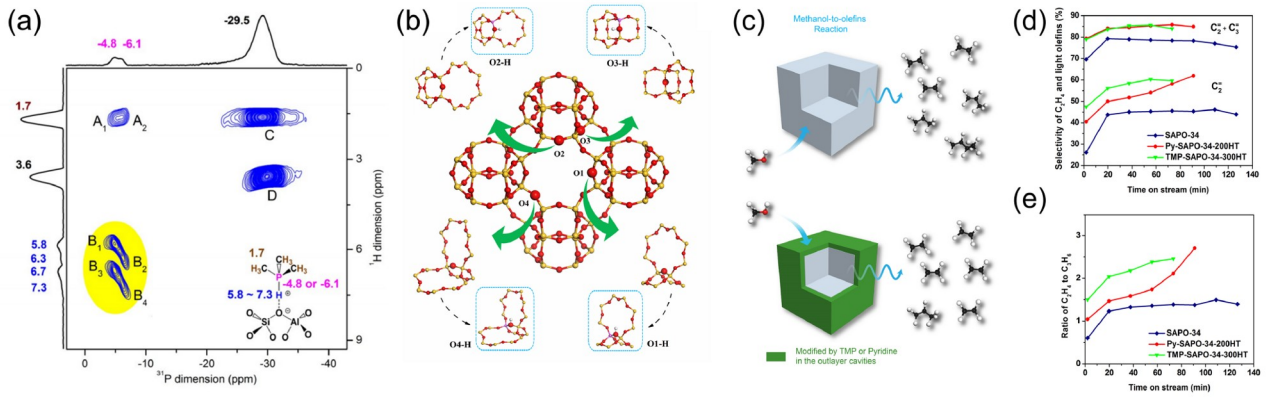

Figure 18 (Color online) (a) The 2D ^{1}H–^{31}P HETCOR NMR spectrum of TMP-SAPO-34–300HT with a contact time of 3 ms. The corresponding projections of ^{1}H and ^{31}P dimensions with chemical shifts (in ppm) are also shown. (b) The CHA crystal geometry. Four O atoms are highlighted by enlargement. O atom locations, O1: two 4-MR and one 8-MR; O2: one 4-MR, one 6-MR and one 8-MR; O3: two 4-MR and one 6-MR; O4: one 4-MR and two 8-MR. The corresponding bridge hydroxy groups O1–H, O2–H, O3–H, and O4–H can be formed when a Si atom is located at an adjacent tetrahedral atom and a proton is attached to these O atoms for charge balance. (c) Schematic diagrams of the strategy for improving light olefins selectivity by imposing extra diffusion limitations via modifying the SAPO-34 catalyst with encapsulation of TMP or pyridine in the outerlayer cavities. (d) The selectivity of ethene and light olefins of methanol conversion over fresh SAPO-34, Py-SAPO-34-200HT, and TMP-SAPO-34-300HT. Py-SAPO-34-200HT: SAPO-34 with the hydrothermally assisted encapsulation of pyridine at 473 K. (e) Ratio of ethene-to-propene [68]. Adapted with permission from ref. 68, Copyright 2020 Wiley-VCH GmbH.

of ssNMR with other time-resolved *in-situ* techniques, such as diffuse reflectance infrared Fourier transform spectroscopy (DRIFTS), synchrotron X-ray, neutron diffraction techniques, and real-time *in-situ* imaging technology, will yield more precise dynamic information on the structure and behavior of catalysts and confined species under real working condition. Furthermore, theoretical calculation methods provide a profound comprehension of catalyst structures and reaction mechanisms at the atomic/molecular levels, thus validating experimental observations and providing complementary information for a comprehensive understanding of the dynamic MTO process under real catalytic conditions. All these fundamental understandings of MTO catalysis will provide strong support for the development and optimization of new-generation catalysts and processes.

Acknowledgements The authors are grateful to the financial support provided by the National Key Research and Development Program of China (2022YFE0116000), the National Natural Science Foundation of China (22241801, 22022202, 22032005, 22288101, 21972142, 21991090, 21991092, and 21991093), and Dalian Outstanding Young Scientist Foundation (2021RJ01).

Conflict of interest The authors declare no conflict of interest.

1 Chang CD, Silvestri AJ. *J Catal*, 1977, 47: 249–259
2 Tian P, Wei Y, Ye M, Liu Z. *ACS Catal*, 2015, 5: 1922–1938
3 Olsbye U, Svelle S, Bjørgen M, Beato P, Janssens TVW, Joensen F, Bordiga S, Lillerud KP. *Angew Chem Int Ed*, 2012, 51: 5810–5831
4 Wan H, Gong N, Liu L. *Sci China Chem*, 2022, 65: 2163–2176
5 Zhang S, Miao D, Ding Y, Li M, Guo S, Zhang Y, Pan X, Bao X. *Sci China Chem*, 2023, 67: 732–740
6 Yang M, Fan D, Wei Y, Tian P, Liu Z. *Adv Mater*, 2019, 31: e1902181
7 Yarulina I, Chowdhury AD, Meirer F, Weckhuysen BM, Gascon J. *Nat Catal*, 2018, 1: 398–411
8 Olsbye U, Svelle S, Lillerud KP, Wei ZH, Chen YY, Li JF, Wang JG, Fan WB. *Chem Soc Rev*, 2015, 44: 7155–7176
9 Wang W, Hunger M. *Acc Chem Res*, 2008, 41: 895–904
10 Haw JF, Song W, Marcus DM, Nicholas JB. *Acc Chem Res*, 2003, 36: 317–326
11 Hwang A, Bhan A. *Acc Chem Res*, 2019, 52: 2647–2656
12 Zhang W, Lin S, Wei Y, Tian P, Ye M, Liu Z. *Natl Sci Rev*, 2023, 10: nwad120
13 Wang C, Xu J, Deng F. *ChemCatChem*, 2020, 12: 965–980
14 Ivanova II, Andriako EP. *Microporous Mesoporous Mater*, 2023, 358: 112363
15 Nishiyama Y, Hou G, Agarwal V, Su Y, Ramamoorthy A. *Chem Rev*, 2023, 123: 918–988
16 Liu B, Wang F, Dou X, Li P, Xiang H, Yang Y, He P. *Sci China Chem*, 2024, 67: 1017–1027
17 Kentgens APM, Verhagen R. *Chem Phys Lett*, 1999, 300: 435–443
18 Hung I, Zhou L, Pourpoint F, Grey CP, Gan Z. *J Am Chem Soc*, 2012, 134: 1898–1901
19 Biedenbänder T, Aladin V, Saeidpour S, Corzilius B. *Chem Rev*, 2022, 122: 9738–9794
20 Duckett SB, Mewis RE. *Acc Chem Res*, 2012, 45: 1247–1257
21 Mastikhin VM, Mudrakovskii IL. *React Kinet Catal Lett*, 1982, 20: 351–355
22 Geschke D, Quillfeldt E. *J Magn Reson*, 1985, 65: 326–331
23 Carpenter TA, Klinowski J, Tilak D, Tennakoon B, Smith CJ, Edwards DC. *J Magn Reson*, 1986, 68: 561–563
24 Xu T, Haw JF. *Top Catal*, 1997, 4: 109–118
25 Xu S, Zhang W, Liu X, Han X, Bao X. *J Am Chem Soc*, 2009, 131: 13722–13727
26 Zhang W, Xu S, Han X, Bao X. *Chem Soc Rev*, 2012, 41: 192–210
27 Ivanova II, Kolyagin YG. *Chem Soc Rev*, 2010, 39: 5018–5050
28 Goguen PW, Xu T, Barich DH, Skloss TW, Song W, Wang Z, Nicholas JB, Haw JF. *J Am Chem Soc*, 1998, 120: 2650–2651
29 Hunger M, Horvath T. *J Chem Soc Chem Commun*, 1995, 1423–1424
30 Jiang Y, Wang W, Reddymarthala V, Huang J, Sulikowski B, Hunger M. *J Catal*, 2006, 238: 21–27
31 Wu X, Wei Y, Liu Z. *Acc Chem Res*, 2023, 56: 2001–2014
32 Zhou H, Gong X, Abou-Hamad E, Ye Y, Zhang X, Ma P, Gascon J, Chowdhury AD. *Angew Chem Int Ed*, 2024, 63: e202318250
33 Chu Y, Yi X, Li C, Sun X, Zheng A. *Chem Sci*, 2018, 9: 6470–6479

34 Yamazaki H, Shima H, Imai H, Yokoi T, Tatsumi T, Kondo JN. *Angew Chem Int Ed*, 2011, 50: 1853–1856
35 Song W, Marcus DM, Fu H, Ehresmann JO, Haw JF. *J Am Chem Soc*, 2002, 124: 3844–3845
36 Wu X, Xu S, Wei Y, Zhang W, Huang J, Xu S, He Y, Lin S, Sun T, Liu Z. *ACS Catal*, 2018, 8: 7356–7361
37 Sun T, Chen W, Xu S, Zheng A, Wu X, Zeng S, Wang N, Meng X, Wei Y, Liu Z. *Chem*, 2021, 7: 2415–2428
38 Lin S, Zhi Y, Chen W, Li H, Zhang W, Lou C, Wu X, Zeng S, Xu S, Xiao J, Zheng A, Wei Y, Liu Z. *J Am Chem Soc*, 2021, 143: 12038–12052
39 Wu X, Chen W, Xu S, Lin S, Sun T, Zheng A, Wei Y, Liu Z. *ACS Cent Sci*, 2021, 7: 681–687
40 Wang C, Chu Y, Xu J, Wang Q, Qi G, Gao P, Zhou X, Deng F. *Angew Chem Int Ed*, 2018, 57: 10197–10201
41 Jiang Y, Hunger M, Wang W. *J Am Chem Soc*, 2006, 128: 11679–11692
42 Li J, Wei Z, Chen Y, Jing B, He Y, Dong M, Jiao H, Li X, Qin Z, Wang J, Fan W. *J Catal*, 2014, 317: 277–283
43 Yang L, Yan T, Wang C, Dai W, Wu G, Hunger M, Fan W, Xie Z, Guan N, Li L. *ACS Catal*, 2019, 9: 6491–6501
44 Liu Y, Müller S, Berger D, Jelic J, Reuter K, Tonigold M, Sanchez-Sanchez M, Lercher JA. *Angew Chem Int Ed*, 2016, 55: 5723–5726
45 Chowdhury AD, Houben K, Whiting GT, Mokhtar M, Asiri AM, Al-Thabaiti SA, Basahel SN, Baldus M, Weckhuysen BM. *Angew Chem Int Ed*, 2016, 55: 15840–15845
46 Wu X, Xu S, Zhang W, Huang J, Li J, Yu B, Wei Y, Liu Z. *Angew Chem Int Ed*, 2017, 56: 9039–9043
47 Gong X, Çağlayan M, Ye Y, Liu K, Gascon J, Dutta Chowdhury A. *Chem Rev*, 2022, 122: 14275–14345
48 Chen W, Yi X, Liu Z, Tang X, Zheng A. *Chem Soc Rev*, 2022, 51: 4337–4385
49 Wang N, Zhi Y, Wei Y, Zhang W, Liu Z, Huang J, Sun T, Xu S, Lin S, He Y, Zheng A, Liu Z. *Nat Commun*, 2020, 11: 1079–1090
50 Li J, Wei Y, Chen J, Tian P, Su X, Xu S, Qi Y, Wang Q, Zhou Y, He Y, Liu Z. *J Am Chem Soc*, 2012, 134: 836–839
51 Xu S, Zheng A, Wei Y, Chen J, Li J, Chu Y, Zhang M, Wang Q, Zhou Y, Wang J, Deng F, Liu Z. *Angew Chem Int Ed*, 2013, 52: 11564–11568
52 Li J, Wei Y, Chen J, Xu S, Tian P, Yang X, Li B, Wang J, Liu Z. *ACS Catal*, 2014, 5: 661–665
53 Zhang M, Xu S, Li J, Wei Y, Gong Y, Chu Y, Zheng A, Wang J, Zhang W, Wu X, Deng F, Liu Z. *J Catal*, 2016, 335: 47–57
54 Zhang M, Xu S, Wei Y, Li J, Chen J, Wang J, Zhang W, Gao S, Li X, Wang C, Liu Z. *RSC Adv*, 2016, 6: 95855–95864
55 Xiao D, Xu S, Brownbill NJ, Paul S, Chen LH, Pawsey S, Aussenac F, Su BL, Han X, Bao X, Liu Z, Blanc F. *Chem Sci*, 2018, 9: 8184–8193
56 Zhang M, Xu S, Wei Y, Li J, Wang J, Zhang W, Gao S, Liu Z. *Chin J Catal*, 2016, 37: 1413–1422
57 Zhang W, Zhi Y, Huang J, Wu X, Zeng S, Xu S, Zheng A, Wei Y, Liu Z. *ACS Catal*, 2019, 9: 7373–7379
58 Zhang W, Xu S, Wei Y, Liu Z. *J Energy Chem*, 2020, 45: 25–30
59 Zhang W, Zhang M, Xu S, Gao S, Wei Y, Liu Z. *ACS Catal*, 2020, 10: 4510–4516
60 Zhou J, Gao M, Zhang J, Liu W, Zhang T, Li H, Xu Z, Ye M, Liu Z. *Nat Commun*, 2021, 12: 17
61 Yu B, Zhang W, Wei Y, Wu X, Sun T, Fan B, Xu S, Liu Z. *Chem Commun*, 2020, 56: 8063–8066
62 Gao S, Yuan J, Liu Z, Lou C, Yu Z, Xu S, Zheng A, Wu P, Wei Y, Liu Z. *J Phys Chem C*, 2021, 125: 6832–6838
63 Gao S, Xu S, Wei Y, Qiao Q, Xu Z, Wu X, Zhang M, He Y, Xu S, Liu Z. *J Catal*, 2018, 367: 306–314
64 Stejskal EO, Tanner JE. *J Chem Phys*, 1965, 42: 288–292
65 Chmelik C, Kärger J. *Chem Soc Rev*, 2010, 39: 4864–4884
66 Schneider D, Mehlhorn D, Zeigermann P, Kärger J, Valiullin R. *Chem Soc Rev*, 2016, 45: 3439–3467
67 Kärger J, Avramovska M, Freude D, Haase J, Hwang S, Valiullin R. *Adsorption*, 2021, 27: 453–484
68 Sun T, Xu S, Xiao D, Liu Z, Li G, Zheng A, Liu W, Xu Z, Cao Y, Guo Q, Wang N, Wei Y, Liu Z. *Angew Chem Int Ed*, 2020, 59: 20672–20681